Direct Modeling of Structures and Segregations Up to Industrial Casting Scales

Ch.-A. GANDIN,[1,2] T. CAROZZANI,[1] H. DIGONNET,[1] S. CHEN,[1] and G. GUILLEMOT[1]

1.—MINES ParisTech, CEMEF, UMR CNRS 7635, CS 10207, 06904 Sophia Antipolis, France. 2.—e-mail: Charles-Andre.Gandin@mines-paristech.fr

Direct modeling of structures and segregations during industrial casting processes is made difficult due to the need for coupling intricate phenomena occurring at multiple length and time scales. Its outputs are, however, required for modeling of further thermomechanical treatments as well as for prediction of in-service properties. The present article presents recent efforts made to integrate microscopic scale concepts taken from physical metallurgy into a macroscopic model. This new model includes macroscopic solution of average conservation equations, mesoscopic scale description of the development of the grain structure, together with microscopic scale consideration for the kinetics of the solid-liquid interfaces and the chemical segregation taking place between phases. Simulations are presented for directional solidification of a cylindrical ingot, a benchmark experiment for macrosegregation in a rectangular cavity, and a surface treatment that mimics the gas tungsten arc welding process. The difficulties of transforming the model into a tool applied for industrial castings are discussed.

INTRODUCTION

Modeling of solidification structures by coupling a finite element (FE) solution of the average energy conservation equation with a cellular automaton (CA) description of the nucleation and growth of the grain structure was introduced two decades ago.[1,2] Initially, it was limited to a two-dimensional (2D) Cartesian approximation but still demonstrated potential for modeling of solidification processing.[3] In particular, examples were shown for investment casting of nickel base alloys. The success of 2D modeling applied to casting of a nickel base component provided a justification for an extension to three-dimensional (3D) modeling,[4] which was later applied to the study of defects formed during directional solidification of single-crystal turbine blade geometries.[5–8]

It was one decade ago that a validated coupling between the CA and FE solvers could be proposed and implemented in two dimensions[9] based on comparison with a front tracking solution of the mushy zone boundaries with undercooling.[10] Coupling with macrosegregation and grain transport was also developed in 2D during this period.[11]

Validation of the macrosegregation coupling was performed via *in situ* real-time x-ray radiography observations in a gallium-5 wt.% indium alloy.[12] The experiment was unique in that a single nucleation event of an almost pure gallium crystal occurred, the growth of which lead to strong macrosegregation of indium induced by natural thermosolutal convection.[13,14]

The successes outlined earlier have given reasons for recent extensions of such models to three dimensions, as well as efforts to derive parallel algorithms.[15] Two applications are presented hereafter, which are compared with experimental data.[16,17] They are complemented with a simulation of surface treatment by welding. The results are used to derive a discussion on the remaining challenges that must be overcome in order to use the CAFE model for systematic applications to solidification processing.

MODELING

Recent efforts for the development of CAFE modeling with respect to 3D parallel implementation and coupling with macrosegregation were

achieved over the last 2 years. Its presentation in the literature is partially given.[16,17] This contribution aims to give a review of the new directions taken with respect to previous models[1–12] as well as to provide with illustration typical achievements. Only a short description of the model is thus provided hereafter:

i. The 3D FE solutions for average enthalpy, average composition, and average momentum, assuming fixed solid phase and constant and equal density for all phases, are computed with parallel solvers. The current implementation is based on the CimLib library,[18] which provides massive parallel tools for solving the FE problem with remeshing based on optimized partitioning methods.[19,20] Adaptation of the FE mesh is regularly performed based on error estimators deduced from the average composition, solid fraction, liquid velocity, and temperature fields.

ii. A second 3D FE mesh, named a CA mesh, is uniquely defined at the beginning of the calculation. It is fixed during the calculations. The CA mesh is used to generate the 3D CA grid, i.e., the assembly of a regular lattice of cubic cells with a size smaller than the CA mesh.

iii. Dynamic allocation of the 3D CA grid is performed automatically based on the CA mesh and the temperature field.[15] Because the CA mesh is kept fixed during the calculation, each of the CA cells is located in a unique and unchanged mesh, identified by a unique CA mesh index. Dynamic allocation of the CA grid is based on the temperature criteria defined and transported on the CA mesh from the FE mesh solution, while de-allocation requires reaching a fully developed structure.

iv. The CA nucleation and growth algorithms to compute the grain structure are similar to those previously published.[4,6] They permit access to the kinetics of the development of the mushy zone boundaries; e.g., for a binary alloy, the limits between the fully liquid melt and the fully solid region within which a mixture between a dendritic solid and an interdendritic liquid are simultaneously present. For that purpose, not only the dendritic grain structure should be simulated but also the eutectic grain structure since they both develop with some undercooling. An extension to the model has thus been implemented to track several grain structures in the same calculation, with independent nucleation and growth kinetics. The fraction of the mushy zone is then fed back by summation over the cells onto the nodes of the CA mesh and finally projected onto the nodes of the FE mesh.

v. The conversion of the average enthalpy, average composition, and fraction of mushy zone into temperature and solid fraction is performed at the nodes of the FE mesh. Compared with previous coupling schemes,[2,6] this provides a major improvement that permits full coherence between all field at the nodes of the FE mesh. It was also shown to reach agreement with converged front tracking methodologies for the mushy zone boundaries.[10,16] It should also be noted that this coupling approach saves computation time.

vi. Coupling with tabulated thermodynamic properties has been implemented.[17] Tabulations of enthalpy are performed for each phase in each structure as a function of temperature and composition, requiring models for internal fraction of phases. In case of full equilibrium, the internal fraction is simply deduced from equilibrium calculations. The present coupling permits a detailed description of the latent heat released during phase transformations while not assuming constant heat capacity or latent heat.

vii. A new storage procedure is developed for tracking the grain structure within each CA mesh during the calculation. The CA grid state is stored onto the hard disk memory and can be read and written any time the CA grid is dynamically allocated. This permits one to start a calculation from an initial state of the grain structure that is not obvious (e.g., initial liquid state in a standard casting process). The advantage for such methodology is obvious when dealing with welding, when an initial grain structure is partially remelted and resolidified over a large region during a small period of the total processing time. It yet requires adaptation of the dynamic allocation procedures mentioned earlier (iii).

APPLICATIONS

Three simulations are presented, the two first being directly compared with temperature measurements, in order to illustrate the possibilities of the 3D CAFE model. Table I provides the list of features given earlier (i–vii) that are demonstrated in each of the following examples.

Directional Solidification of a Rod

The standard example concerns directional solidification of a binary metallic alloy. It is regularly used in the literature as a test case for modeling of grain structures,[21–24] although so far not in three dimensions. It also corresponds to experimental results in Al-Si alloys that are well documented.[10,25] The ingot geometry is a 70-mm-diameter cylinder that lies vertically on a cooled chill. The measured length of the cylinder at the end of the solidification is 170 mm. Temperature probes are localized at 20, 40, 60, 80, 100, 120, and 140 mm from the bottom of the ingot. They permit extrapolation of temperature evolution in the alloy at the interface with the chill, i.e., at position 0 mm. Such a computed cooling curve is used as a Dirichlet boundary condition

Table I. Numerical parameters and CPU times of the CAFE simulations

Case	Figures 1 and 2 Al-7 wt.%Si Cylinder	Figures 3 and 4 Sn-3 wt.%Pb Cavity	Figure 5 Steel Coupon
FE domain size (m)	$0.07\varnothing \times 0.173$	$0.1 \times 0.06 \times 0.01$	$0.35 \times 0.15 \times 0.012$
FE mesh size (m)	5×10^{-3}	1.2×10^{-3}	5×10^{-3} (initial)
Time step (s)	0.1	0.1	0.5
FE solvers	Energy	Energy solute mass liquid momentum	Energy
CA domain size (m)	$0.07\varnothing \times 0.173^{a}$	$0.1 \times 0.06 \times 0.01^{a}$	$0.27 \times 0.09 \times 0.006$
CA mesh size (m)	5×10^{-3}	1.2×10^{-3}	3×10^{-3}
Cell size (m)	2.5×10^{-4}	2×10^{-4}	8×10^{-5}
CAFE features (see text)	i–v	i–iii, v, vi	i–iii, vii
Number of processors	16	64	32
Computation time	3 days, 6 hours	5 days	2 days, 16 hours

[a]Same FE and CA meshes.

at the lower surface of the vertical cylindrical geometry.

In the absence of a mechanical solution, phase flow cannot be computed. Consequently, there is no possibility for direct simulation of shrinkage and thermal contractions due to phase transformation and cooling, and the time evolution position of the top free surface of the alloy with the air is not computed. To account for shrinkage, a 173-mm-height simulation domain is chosen, which is slightly longer than the final measured ingot length. A small heat flux, equal to 3000 W m^{-2}, is also imposed on the top surface of the cylindrical geometry during the first 900 s of the simulation, while the cylinder surfaces are taken adiabatic. The initial temperature is directly extracted from the measurement at the beginning of the solidification experiment. The latter optimizations, as well as the growth kinetics of the dendritic structure, the values of the specific heat, conductivity, and other material properties, are well documented and justified elsewhere.[10,25] This first simple test is restricted to heat diffusion, fully coupled with grain structure development. The numerical parameters for the simulations are given in Table I.

Figure 1 (See video available in Electronic Supplementary Material) provides a 3D representation of the predicted time sequence of the development of the dendritic grain structure. As shown, predicted grain shapes are columnar (elongated) in the bottom part of the ingot and equiaxed (more isotropic shape) in the top part. A columnar-to-equiaxed transition (CET) is thus modeled, which is similar to the experimental observation.[10,25] Figure 2 also shows the predicted cooling curves at the same position as the thermocouples, from 20 mm to 140 mm. The curve at position 0 mm indicates the boundary condition imposed at the bottom of the cylindrical domain. The agreement is overall very good, much better than the result reached previously with 2D approximations.[2] This is particularly true when considering the detailed time evolution of the temperature within a few degrees below the

liquidus isotherm of the alloy (618°C at the maximum temperature range in Fig. 2). A recalescence is revealed at position 140 mm that could be directly compared with measurement.[16] Such recalescence could not be predicted without coupling the FE solution for heat flow with structure prediction. The same comment applies for the cooling rate changes at lower positions (e.g., 120 and 100 mm), which is identified just below the liquidus isotherm. Finally, one could also notice that, while the eutectic temperature (577°C) for this system is within the temperature range of Fig. 2, the last cooling rate change that reveals the final eutectic solidification takes place at a lower temperature (e.g., 574°C at 140 mm). This difference represents the eutectic undercooling taken into account in this simulation, by also tracking the eutectic grain structure that develops inside the mushy zone. The eutectic structure is columnar in the present simulation and is not shown in Fig. 1, but the influence of considering a eutectic structure in a low cooling rate configuration was already demonstrated to predict recalescence upon eutectic growth.[15]

Several difficulties still exist when comparing the simulation results with observations. In fact, the position of the CET is not very well predicted as it happens sooner in the simulation—108.3 mm—compared with measurement—118 mm. Moreover, the size of the equiaxed grain structure could not be predicted as small as it was measured. These differences could be explained by several causes. First the simulation does not include grain sedimentation, which may play an important role on the average grain size. Second, the undercooling of the columnar dendrite tips could be decreased by shrinkage-induced fluid flow, thus, delaying the nucleation of heterogeneous particles. Finally, it was suggested that the CET could be induced as a result of dendrite fragmentation taking part at the columnar growth front when the temperature gradient in the liquid becomes sufficiently low.[10,21,22,25] These phenomena are not considered by the present CAFE simulation.

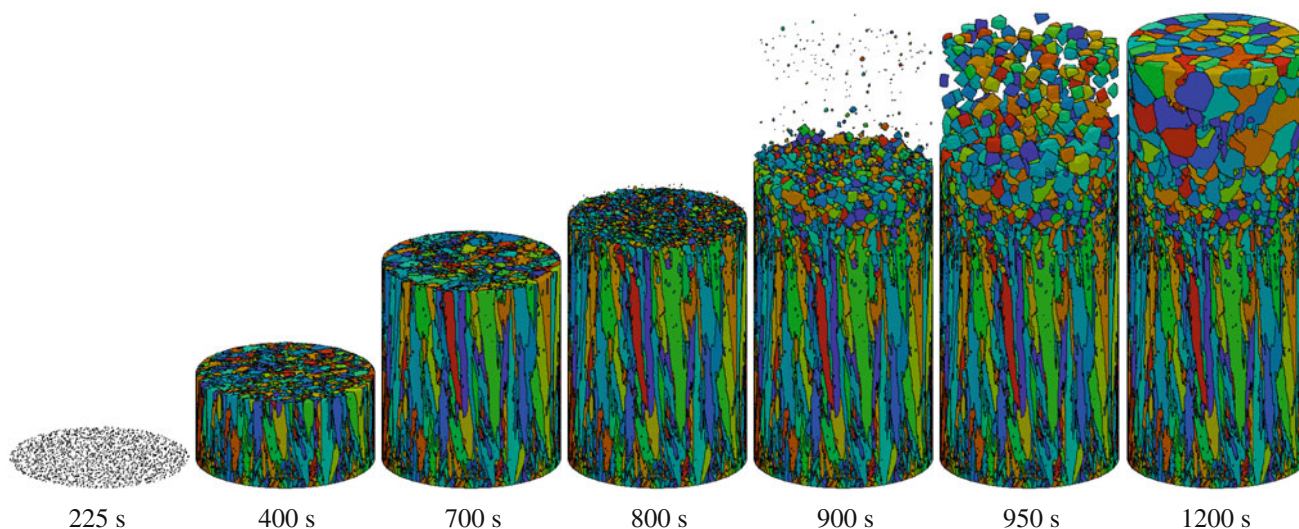| 225 s | 400 s | 700 s | 800 s | 900 s | 950 s | 1200 s |

Fig. 1. CAFE simulation of the formation of the grain structure during solidification of a 173-mm-height, 70-mm-diameter Al-7wt.%Si rod. The oriented structure at the bottom of the ingot is stopped by the growth of grains nucleated in the liquid, giving rise to the so-called columnar-to-equiaxed transition[16] (See video available in Electronic Supplementary Material).
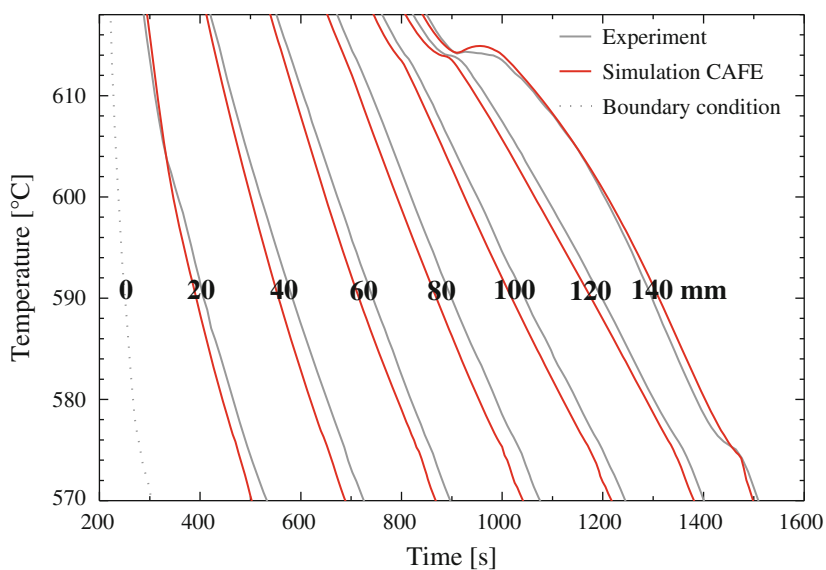

Fig. 2. Cooling curves at labeled distances defined from the bottom surface of the Al-7wt.%Si rod displayed in Fig. 1 (gray) recorded[25] and (continuous red) computed with the CAFE model.[16] The doted curve at position labeled 0 mm (i.e., at the bottom of the simulation domain) is used as the boundary condition for the FE energy solver.

Solidification of a Rectangular Cavity

The second application makes use of most of the new developments. Not only does it consider a full coupling scheme between the CA prediction of the dendritic grain structure with the FE solution for energy, momentum, and solute mass conservations, but it also makes use of a full set of tabulated thermodynamic properties for all phases formed during cooling, from the initial temperature above the liquidus of the alloy down to room temperature. The situation also corresponds to a well-documented experiment provided elsewhere.[17,26]

The domain consists of a rectangular cavity with dimensions 100 mm width × 60 mm height × 10 mm thick. The opposite smallest left-hand-side (LHS) and right-hand-side (RHS) surfaces of the cavity, with dimensions 60 mm × 10 mm, are positioned vertically and maintained into contact with heat exchangers with controlled temperatures. Adiabatic conditions are applied on all other surfaces. Four thermocouples are identified with symbol × in Fig. 3 (See video available in Electronic Supplementary Material) and a colored label, L21, L24, L27, and L30. They are part of a network of
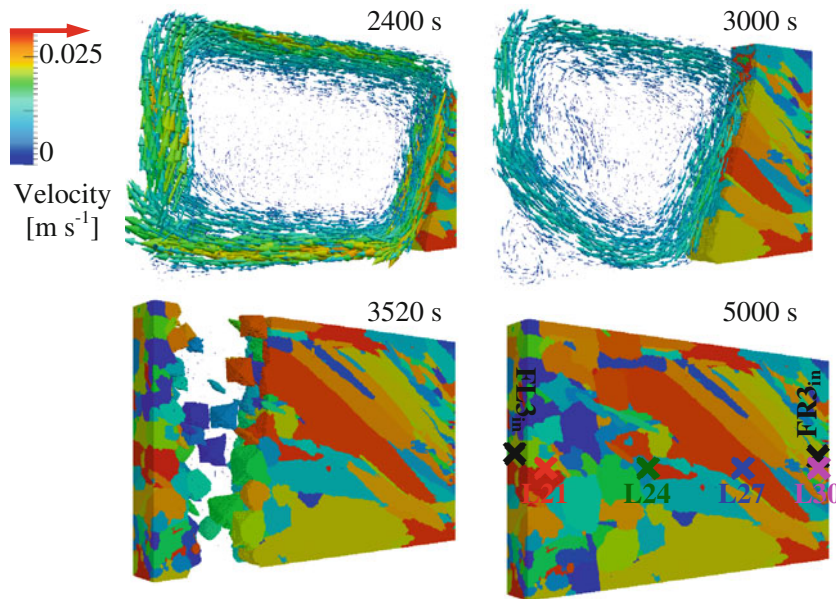
Fig. 3. CAFE simulation of the formation of the grain structure during solidification of a 100-mm-width × 60-mm-height × 10-mm-thick Sn-3wt.%Pb cavity. Arrows provide with the flow direction while its color and length are proportional to the velocity.[17] Labels refer to thermocouples L21, L24, L27, and L30 located on the surface of the cavity, at midheight, and at distances 5, 35, 65, and 95 mm from the left-hand-side vertical surface, respectively. Positions FL3$_{in}$ and FR3$_{in}$ are also labeled the center of the left and right vertical surfaces, respectively (See video available in Electronic Supplementary Material).

50 thermocouples located on the surface of the cavity, plus 6 thermocouples located in each heat exchanger. This dense network of measurements is used to determine the temperature evolution applied as Dirichlet condition on the RHS and LHS smallest vertical surfaces of the cavity. Such cooling histories are provided as dotted gray curves in Fig. 4 at positions labeled FR3$_{in}$ and FL3$_{in}$ in Fig. 3.

A Sn-3 wt.%Pb alloy is placed in the cavity. From an initial melted and homogenized liquid at an average temperature of 531.75 K (i.e., corresponding to time equal 0 s in Figs. 3 and 4), the LHS heat exchanger is heated up while the RHS heat exchanger is cooled down while remaining above the liquidus of the alloy (501.28 K). These temperatures are maintained for 1000 s so that a stable natural convection regime settles. Finally, the RHS and LHS heat exchangers are simultaneously cooled down at -0.03 K s^{-1} until complete solidification, so that a 40 K difference is maintained between the LHS and RHS heat exchangers during the entire solidification experiment. Figure 3 shows the fluid flow induced by natural convection while the solidification structure just started to form at 2400 s. At this time, the measurements in Fig. 4 reveal no temperature gradient in the melt between thermocouples L24 and L27 due to temperature homogenization thanks to convection. In comparison, thermocouples L21 and L24 as well as L27 and L30 show clear differences that are maintained along the entire cooling sequence. In the liquid state, a temperature gradient is thus only concentrated in the vicinity of the heat exchangers. The differences

between L24 and L27 only start to appear when the solidification front reaches position L27 at about 2800 s. Then the liquid flow progressively vanishes and cooling of L27 significantly increases and departs from the shape of the cooling curve of L24. The strong interaction of the liquid flow with the development of the grain structure is clearly revealed in Fig. 3 at time 3000 s. The convection loop progressively moves toward the LHS hotter boundary of the domain upon growth of a columnar grain structure from the RHS cold boundary. During this displacement, fluid flow is maintained in the mushy zone. Upon further cooling, the volume of liquid that becomes undercooled increases while the temperature gradient in the melt decreases. This is shown in Fig. 4 by the decrease of the temperature difference between L21 and L24 before 3400 s. Nucleation of new grains can take place in the melt as shown at time 3520 s in Fig. 3, thus, leading to a recalescence measured and predicted at position L21.[17]

Unlike for the case of directional solidification shown in the previous example, the predicted columnar grain structure is not aligned with the main heat flow direction (normal to the vertical lateral surfaces of the cavity). The overall upward inclined growth direction of the grains corresponds to the installation of a texture due to the dependence of the growth undercooling with the crystallographic orientation of each individual grain. The explanation is due to the introduction of the fluid flow direction with respect to the <100> growth directions of the grains for the computation of the growth kinetics. Because the flow shown in Fig. 3 is
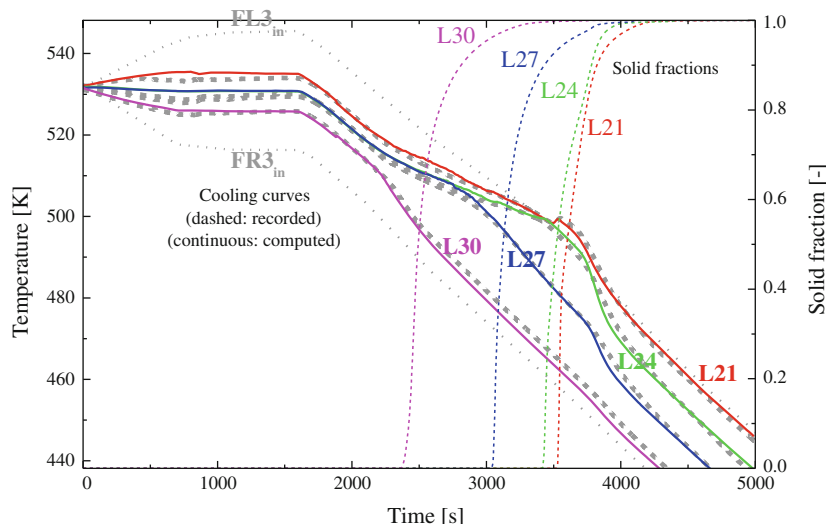
Fig. 4. Cooling curves at positions defined on the computed metallographic grain structure of the Sn-3wt.%Pb rectangular cavity displayed in Fig. 3 (dashed gray) recorded[26] and (continuous colored) computed with the CAFE model. The dotted curves labeled FL3$_{in}$ and FR3$_{in}$ are used as boundary conditions for the energy solver on the smallest vertical right-hand-side and left-hand-side faces of the simulation domain, respectively. Additional curves (thin dashed colored) show the time evolution of the fraction of solid at positions of the simulated cooling curves.

going downward along the growth front, the growth directions of the grains that are opposite to the flow can adopt a smaller undercooling. They extend faster in the undercooled liquid and lead to the present grain selection and texture. This trend is confirmed by the metallographic inspection of the surface of the ingot. Predictions also include a macrosegregation map that can be compared with measurements conducted with x-ray imaging as well as by inductively coupled plasma (ICP) spectrometry.[17] In the present experimental configuration, the origin of macrosegregation is the thermosolutal convection that leads to accumulation of the segregated specie, Pb, at the bottom LHS of the cavity. The transport of the equiaxed grains due to gravity and convection is not implemented in the 3D CAFE model, despite its feasibility demonstrated in previous work,[11] nor is the effect of deformation and shrinkage. The transport of the grains can be reasonably neglected in the present experiment because the structure is mainly of a columnar nature. As previously discussed, the equiaxed grains shown in the left-hand-side of Fig. 3 may also have originated from fragmentation of the columnar dendritic front when it slowed down and propagated in a liquid with no temperature gradient. If this was the case, the equiaxed grains formed very close to the growth front and were likely to experience very small transport.

Gas Tungsten Arc Welding

The previous applications started from initial fully liquid conditions, i.e., above the liquidus temperature of the alloys. However, some situations or processes require modeling of melting. A start from a solid structure is then needed, obviously present when the initial temperature is below the liquidus of the alloy. For instance, in welding, the specimen is at low temperature prior to being heated and melted by a heat source, and it is then solidified. A typical example is provided by a surface treatment using the gas tungsten arc welding process. The heat source moves above a surface and partially melts the material, usually made of a fine equiaxed structure. This initial structure can be more or less textured depending on the previous forming steps used. For instance, rolling is known to produce an initial texture that should then be accounted for. Epitaxial growth then takes place from the partly melted grains and propagates their crystallographic orientation. In case of no nucleation of new equiaxed grains in the melt, a new columnar structure can be created. A grain selection process occurs. Consequently, the grain sizes in the new columnar structure are larger than in the base metal.

The difficulty with this situation is the need to access anytime the structure of a simulation domain that can be large. The CA grid structure is too large to be loaded into the memory of computers, and special methods must be developed. This is why dynamic allocation/deallocation techniques were developed as discussed in the modeling section (iii). The last new additional developments permit storage of the information on the hard disk based on the CA grid built on the fixed CA mesh. The model reads and stores information concerning the structure at any time during a simulation. Thus, when the nodes of the CA mesh fulfill conditions for dynamic allocation, the CA grid information that contains the initial structure can be read from the hard disk and used as an initial condition for the calculation. After
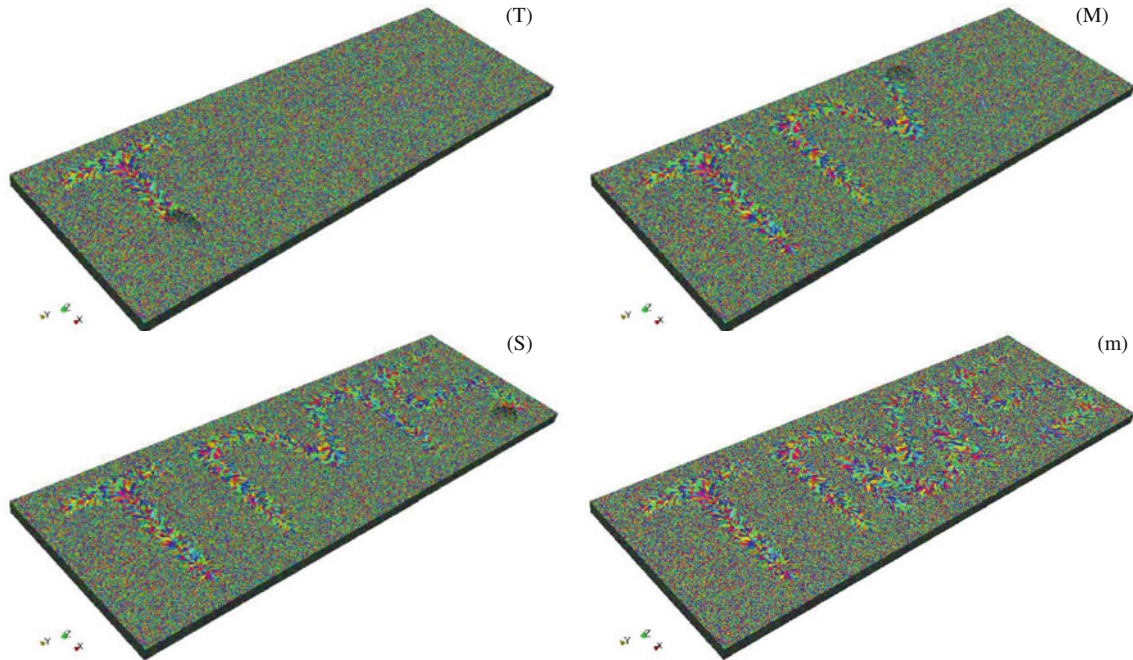
Fig. 5. Simulated gas tungsten arc welding heat treatment on a steel coupon with dimensions $27 \times 9 \times 0.6$ cm^3: the initial very fine equiaxed structure is partially remelted and resolidified with a columnar structure, revealing the imposed letter sequence for the pattern of the heat source: (T) T, (M) M and (S) S and (m) TMS. The heat source is switched off at the end of a letter prior to being moved at the beginning of the next one (See video available in Electronic Supplementary Material).

the calculation, deallocation takes place and the updated information is restored on the hard disk. With this method, the structure can be melted and solidified as many times as required, which is a definite advantage for multipass welding processes. Of course this means that the dynamic allocation procedure initially defined for solidification calculations alone when going down to the liquidus temperature requires an adaptation to permit activation of the structure.

Figure 5 (See video available in Electronic Supplementary Material) provides a typical example. A heat source is moved on top of the surface of a steel coupon at 2 mm s^{-1}. A Gaussian distribution is adopted with a 3000 W power and a standard deviation radius equal to 0.3 cm. The coupon is also cooled down by convection using a heat transfer coefficient equal to 100 W m^{-2} K^{-1} for describing exchanges with the surrounding gas at 20°C, as well as by radiation with emissivity coefficient taken equal to 0.5. The steel coupon is $0.35 \times 0.15 \times 0.012$ m^3, thus, corresponding to approximately the same volume as the case provided in Fig. 1. But the CA mesh is chosen smaller, i.e., $0.27 \times 0.09 \times 0.006$ m^3, so as to limit the volume of the domain considered for grain structure calculations, and yet large enough to encompass the entire path of the heat source. The initial grain structure is computed equiaxed with density 10^{11} m^{-3} (15 millions grains) and stored on the hard disk. When at least one node of a given element of the CA mesh reaches the liquidus temperature of the alloy (1481°C), this

element is activated and the corresponding structure is loaded for calculation. It is then deactivated when the temperature of all its nodes become lower than the liquidus temperature and the mushy zone is fully developed. The pattern followed by the heat source in Fig. 5 reveals the size of the weld pool and the growth of columnar grains that replace the initial equiaxed grain structure. Upon growth, the orientation of the columnar grains follows the heat source direction and writes a series of letters that form the acronym of this journal's publisher. The number of cells for this calculation reaches 285 millions, a number that would have been impossible to load into the memory of a single computer.

DISCUSSION/CONCLUSIONS

New developments of the 3D CAFE model based on parallel implementations have shown the ability to deal with reasonably large volumes of computations. With its last functionality to store and load local information from the hard disk, the limit in term of domain size is further increased. It should be reminded that the model was initially developed in 3D for application to the investment casting process applied to turbine blades geometries.[6,7] The reason was not only the need for a good control of the grain structure, especially for single-crystal turbine blades, but also the fact that the model was particularly well adapted to a small volume of metallic alloys. With the present new calculations, a demonstration has been made that the develop-

ments can be used on much larger domain sizes with reasonable computational time and resources as shown in Table I.

The new coupling methodology should also be emphasized. The only information used from the CA calculation to feed back the FE solution is the fraction of mushy zone. Thus, with addition of the average enthalpy and composition, conversion into temperature and fraction of phases can be made in a coherent manner at the nodes of the FE mesh. Iterations between computation of the CA grain structure and the FE solution has even been tested.[16] Although it was found to improve convergence efficiency, the memory usage for the CA method then doubled and the computation time was also increased. Both of these deficiencies are not convenient in the case of large computations.

Improvements have also been implemented with respect to the nature of the grain structure. The development of the eutectic grain structure has been added on top of the dendritic grain structure. This is shown to further complicate the solidification path that then not only depends on the primary dendritic undercooling but also on the secondary eutectic one. It also explains why the coupling with a more detailed description of the thermodynamic properties was considered since the properties of several undercooled phases is now added.

A list of remaining difficulties for applications and systematic use of the 3D CAFE model in an industrial setting is given below:

– Implementation into a commercial code is required. While some already exist, they do not include the previously listed new developments and are thus still limited to small casting volumes if a reasonable cell size is to be used.
– Visualization becomes a limitation due to the large number of cells that must be represented, thus, requiring special tools for reconstructing the structure.
– Coupling with a solid velocity field due to thermomechanical deformation of solid transport is required and does not yet exist.
– Material parameters, such as the interfacial energies for the growth kinetics computation or the diffusion data for species, are often not available and need to be retrieved from experimental data.
– Further improvements of the coupling with local microscopic phenomena are still required. This could benefit from links with other modeling methodologies. In particular, one should consider the computation of the growth kinetics and branching mechanisms in nontrivial liquid solute fields that result from the development of a dendritic network,[27,28] as well as advanced microsegregation models accounting for solid diffusion and multiple phases concomitantly formed from the melt.[29–33]

– Full demonstration of the importance of the grain structure on the final properties of industrial alloys can only be achieved by advance coupling with further thermomechanical processing, as demonstrated in previous efforts.[34,35]

While the present contribution demonstrates one more step toward achieving a industrial process scale prediction of grain structure in casting and solidification processes, several challenges need to be overcome before the 3D CAFE model can be routinely used.

ELECTRONIC SUPPLEMENTARY MATERIAL

The online version of this article (doi:10.1007/s11837-013-0679-z) contains supplementary material, which is available to authorized users.

REFERENCES

1. M. Rappaz and Ch.-A Gandin, *Acta Metall. Mater.* 41, 345 (1993).
2. Ch.-A Gandin and M. Rappaz, *Acta Metall. Mater.* 42, 2233 (1994).
3. M. Rappaz, Ch.-A Gandin, J.-L. Desbiolles, and Ph. Thévoz, *Metall. Trans. A* 27, 695 (1996).
4. Ch.-A Gandin and M. Rappaz, *Acta Mater.* 45, 2187 (1997).
5. Ch.-A Gandin, M. Rappaz, D. West, and B.L. Adams, *Metall. Trans.* 26A, 1543 (1995).
6. Ch.-A Gandin, J.-L. Desbiolles, M. Rappaz, and Ph. Thévoz, *Metall. Mater. Trans. A* 30, 3153 (1999).
7. P. Carter, D.C. Cox, Ch.-A Gandin, and R.C. Reed, *Mater. Sci. Eng. A-Struct.* 280, 233 (2000).
8. H. Takatani, Ch.-A Gandin, and M. Rappaz, *Acta Mater.* 48, 675 (2000).
9. G. Guillemot, Ch.-A Gandin, H. Combeau, and R. Heringer, *Modell. Simul. Mater. Sci. Eng.* 12, 545 (2004).
10. Ch.-A. Gandin, *Acta Mater.* 48, 2483 (2000).
11. G. Guillemot, Ch.-A. Gandin, and H. Combeau, *ISIJ Int.* 46, 880 (2006).
12. G. Guillemot, Ch.-A. Gandin, and M. Bellet, *J. Cryst. Growth* 303, 58 (2007).
13. H. Yin and J.N. Koster, *J. Cryst. Growth* 205, 590 (1999).
14. H. Yin and J.N. Koster, *J. Alloy. Compd.* 352, 197 (2003).
15. T. Carozzani (Ph.D. thesis, MINES ParisTech, Paris, France, 2012).
16. T. Carozzani, H. Digonnet, and Ch.-A. Gandin, *Modell. Simul. Mater. Sci. Eng.* 20, 015010 (2012).
17. T. Carozzani, Ch.-A. Gandin, H. Digonnet, M. Bellet, K. Zaidat, and F. Fautrelle, *Metall. Mater. Trans. A* 44, 873 (2013).
18. Y. Mesri, H. Digonnet, and T. Coupez, *Eur. J. Comp. Mech.* 18, 669 (2009).
19. H. Digonnet (Ph.D. thesis, Ecole Nationale Supérieure des Mines de Paris, Paris, France, 2001).
20. A. Basermann, J. Clinckemaillie, T. Coupez, J. Fingberg, H. Digonnet, R. Ducloux, J.-M. Gratien, U. Hartmann, G. Lonsdale, B. Maerten, D. Roose, and C. Walshaw, *Appl. Math. Model.* 25, 83 (2000).
21. M.A. Martorano, C. Beckermann, and C.A. Gandin, *Metall. Mater. Trans. A* 34, 1657 (2003).
22. M.A. Martorano, C. Beckermann, and C.A. Gandin, *Metall. Mater. Trans. A* 35, 1915 (2004).
23. V.B. Biscuola and M.A. Martorano, *Metall. Mater. Trans. A* 39, 2885 (2008).
24. S. McFadden, D.J. Browne, and Gandin Ch.-A., *Metall. Mater. Trans. A* 40, 662 (2009).

25. Ch.-A. Gandin, *ISIJ Int*. 40, 971 (2000).
26. L. Hachani, B. Saadi, X.D. Wang, A. Nouri, K. Zaidat, A. Belgacem Bouzida, L. Ayouni-Derouiche, G. Raimondi, and Y. Fautrelle, *Int. J. Heat Mass. Transfer* 55, 1986 (2012).
27. Ch–A Gandin, M. Eshelman, and R. Trivedi, *Metall. Mater. Trans. A* 27, 2727 (1996).
28. D. Tourret and A. Karma, *IOP Conf. Ser.: Mater. Sci. Eng*. 33, 012095 (2012).
29. Ch.-A. Gandin, S. Mosbah, Th. Volkmann, and D.M. Herlach, *Acta Mater*. 56, 3023 (2008).
30. S. Mosbah, M. Bellet, and Ch–A. Gandin, *Metall. Mater. Trans. A* 41, 651 (2010).
31. Ch.-A. Gandin, *Compte. Rendus Phys.* 11, 216 (2010).
32. D. Tourret, Ch.-A. Gandin, Th. Volkmann, and D.M. Herlach, *Acta Mater.* 59, 4665 (2011).
33. D. Tourret, G. Reinhart, Ch–A Gandin, G.N. Iles, U. Dahlborg, M. Calvo-Dahlborg, and C.M. Bao, *Acta Mater.* 59, 6658 (2011).
34. Ch–A Gandin, Y. Bréchet, M. Rappaz, G. Canova, M. Ashby, and H. Shercliff, *Acta Mater.* 50, 901 (2002).
35. Ch.-A. Gandin and A. Jacot, *Acta Mater*. 55, 2539 (2007).